University of Reading

Using "ghost front" to predict the arrival time and speed of CMEs at Venus and Earth

Article

Published Version

Creative Commons: Attribution 4.0 (CC-BY)

Open Access

Chi, Y., Scott, C., Shen, C., Owens, M., Lang, M., Xu, M., Zhong, Z., Zhang, J., Wang, Y. and Lockwood, M. (2020) Using "ghost front" to predict the arrival time and speed of CMEs at Venus and Earth. The Astrophysical Journal, 899 (2). 143. ISSN 0004-637X doi: https://doi.org/10.3847/1538-4357/aba95a Available at http://centaur.reading.ac.uk/91938/

It is advisable to refer to the publisher's version if you intend to cite from the work. See Guidance on citing.

To link to this article DOI: http://dx.doi.org/10.3847/1538-4357/aba95a

Publisher: American Astronomical Society

All outputs in CentAUR are protected by Intellectual Property Rights law, including copyright law. Copyright and IPR is retained by the creators or other copyright holders. Terms and conditions for use of this material are defined in

the End User Agreement.

www.reading.ac.uk/centaur

CentAUR

Central Archive at the University of Reading

Reading's research outputs online

The Astrophysical Journal, 899:143 (14pp), 2020 August 20 https://doi.org/10.3847/1538-4357/aba95a
© 2020. The Author(s). Published by the American Astronomical Society.
OPEN ACCESS

Using the "Ghost Front" to Predict the Arrival Time and Speed of CMEs at Venus and Earth

Yutian Chi[1,2,3], Christopher Scott[2], Chenglong Shen[1,3], Mathew Owens[2], Matthew Lang[2], Mengjiao Xu[1], Zhihui Zhong[1], Jie Zhang[4], Yuming Wang[1], and Mike Lockwood[2]
[1] CAS Key Laboratory of Geospace Environment, Department of Geophysics and Planetary Sciences, University of Science and Technology of China, Hefei, People's Republic of China
[2] Department of Meteorology, University of Reading, Berkshire, UK; chris.scott@reading.ac.uk
[3] CAS Center for Excellence in Comparative Planetology, University of Science and Technology of China, Hefei, People's Republic of China; clshen@ustc.edu.cn
[4] Department of Physics and Astronomy, George Mason University, Fairfax, VA 22030, USA
Received 2020 April 28; revised 2020 July 23; accepted 2020 July 23; published 2020 August 25

Abstract

Using in situ measurements and remote-sensing observations, we study two coronal mass ejections (CMEs) that left the Sun on 2012 June 13–14 and impacted both Venus and Earth while the planets were in close radial alignment. The two CMEs generate multiple fronts in Solar Terrestrial Relations Observatory (STEREO)/Heliospheric Imager (HI) images, which can also be observed in the "J-map" as bifurcated features. We present the "ghost front" model to combine remote observations from STEREO/SECCHI and in situ observations from the Wind and Venus Express (VEX) spacecraft, and to derive the kinematics and propagation directions of the CMEs. By fitting the observations of multiple fronts to a kinematically evolving flux rope model and assuming the CMEs undergo deceleration through frictional drag with a steady-state solar wind, we confirm that the outer and inner fronts of the CMEs as detected in HI images are consistent with peaks in Thomson scattered light returned from the flank and nose of a single front for each CME. An interaction takes place between CME-1 and CME-2 that can be observed in the HI-1 field of view (FOV) before CME-1 encounters Venus. The multipoint in situ observations of the shock–CME interaction event serve as further evidence of the interaction between CMEs. The arrival times calculated from the ghost front model are within 2.5 hr of those observed at VEX and Wind. Our analysis indicates that ghost fronts could provide information about the longitudinally extended shape of the CME in the FOV of HI-1, which can be used to improve the forecast of interplanetary CME arrival time at Earth.

Unified Astronomy Thesaurus concepts: Heliosphere (711); Solar coronal mass ejections (310); Space weather (2037)

1. Introduction

Coronal mass ejections (CMEs) are large-scale eruptions of magnetized plasma transferring huge energies ($\sim 10^{24} J$) from the lower solar corona into interplanetary space. Interplanetary CMEs (ICMEs), the interplanetary manifestations of CMEs, are the major cause of severe space weather (Gosling et al. 1991; Zhang et al. 2007; Richardson & Cane 2012). The potential to be hazardous to ground- and space-based technology (Eastwood et al. 2017) makes ICMEs of critical importance to space weather studies. The precise forecasting of arrival time of the ICME is an important basis for making usable forecasts of space weather events on a cost/loss basis, especially if supplemented with information about the speed of the event on arrival (Owens et al. 2020b). The latter can be found by allowing for the interaction of the event with the ambient interplanetary medium but not from the transit time alone (and assuming the event arrives with its average speed). Before 2006, it was not possible to continuously track CMEs and hence directly link near-Sun observations with their properties as measured in situ. A milestone in the investigation of CMEs propagating through the heliosphere to 1 au is the Solar Terrestrial Relations Observatory (STEREO; Kaiser et al. 2008) mission. The two coronagraphs (COR1 and COR2) and Heliospheric Imagers (HIs; Eyles et al. 2009) on board the two STEREO spacecraft for the first time provide an invaluable platform for studying CME propagation and evolution from 1 $R_{\rm Sun}$ to $\sim$1 au (Howard et al. 2008). The HI instruments are unique in their ability to image plasma density enhancements, such as CMEs, through interplanetary space, providing important information about the geometry, velocity, acceleration/deceleration, and direction of CMEs. The intensities seen in each pixel of an HI image result from sunlight scattered by free electrons via Thomson scattering integrated along the line of sight.

CMEs are often observed with multiple fronts in brightness in the HI-1 cameras of the STEREO satellites that have a field of view (FOV) near the Sun. Because of their wide observation angles and scattering effects, the projection of scattered light from a three-dimensional structure onto a two-dimensional image makes it challenging to associate the complex features in HI images with the different parts of a CME (Vourlidas & Howard 2006; Lugaz et al. 2008, 2012). Some authors have interpreted the outer fronts as the position of a shock ahead of the ejecta, existing in white-light images as a sharp edge all the way around the CME front (Liu et al. 2010; Maloney & Gallagher 2011; Poomvises et al. 2012; Hess & Zhang 2014). This assumption can well explain parts of some CME events with multiple fronts observed by HI images. However, only about half of the ICMEs can drive a fast upstream shock, according to the statistical result of Chi et al. (2016). For some multiple-front events, there are no radiowave interplanetary

Original content from this work may be used under the terms of the Creative Commons Attribution 4.0 licence. Any further distribution of this work must maintain attribution to the author(s) and the title of the work, journal citation and DOI.

scintillation nor in situ data available to corroborate this assumption (Maloney & Gallagher 2011; Scott et al. 2019). The relation between multiple fronts from HI and in situ plasma and magnetic field characteristics was also analyzed by Möstl et al. (2009), who considered them as a shock–sheath and CME core structure. Manchester et al. (2008) explained the appearance of the multiple fronts in the HI-2 FOV (further from the Sun) as being due to the CME front making multiple crossings of the Thomson sphere. However, such intersections cannot well explain the multiple fronts seen at much lower elongations in HI-1 images, or the large longitudinal separations (>180°) between the two spacecraft (the angle bracketing the Earth). The new correlation-aided reconstruction method (Li et al. 2018), which retrieves 3D solar wind transients from STEREO/HI-1 image data, also could be used to reconstruct the two fronts observed in HI-1. Scott et al. (2019) proposed an explanation in which the multiple CME fronts observed in HI-1's FOV were interpreted as two sections of the same CME front. In the case that they analyzed, a CME had two fronts in HI images that were similar in shape but separated by a few degrees in elongation, and the authors demonstrated that the elongation of these two fronts was consistent with the projection of light scattered from the nose and flank of a single CME front. For the case presented, the leading edge of the CME in the HI images corresponded to the flank of the CME that formed a tangent to the observer's line of sight, because of the enhancement in Thomson scattering along this line of sight (Morrill et al. 2009). In addition, a discrete, relatively dense region of plasma accumulating at the nose of a CME is associated with the secondary bright "ghost" front in HI-1 images. We note that the ghost front model does not require the presence of a shock. The term "CME" in this paper is used to describe both the shock and sheath regions ahead of the erupting plasma bubble as well as the bubble itself. That the two fronts are similar in shape and separated by a few degrees in elongation adds strength to the argument that these two features are part of the same extended structure. Although not considered by Scott et al. (2019) in their initial study, the ghost front model not only has the potential to provide information about the longitudinal shape of a CME in the FOV of HI-1, but this improved description of the shape of the CME front can also be used to improve the forecast of the arrival time of an ICME at Earth. In the current paper, we combine the ghost front model technique with an assumed drag-based interaction with the solar wind to investigate the propagation of two Earth-impacting CMEs.

Several techniques have been developed to determine CME kinematics and predict the arrival time of CMEs in the near-Earth space, usually based on the observed time-elongation evolution of a CME (known as a J-map, Sheeley et al. 1999). The "fixed phi" (Fϕ) method (Sheeley et al. 1999; Sheeley & Rouillard 2010) assumes that the CME front is a pointlike source along a particular radial line from the Sun. The harmonic mean (HM) method (Lugaz et al. 2009) assumes that the CME front is an expanding sphere with one edge anchored at the Sun. The self-similar expansion (SSE) technique (Davies et al. 2012) assumes a circular CME front expanding with a constant angular width. This latter technique introduces the CME half-width as an additional free parameter. By setting this to 0° or 180°, the SSE technique can emulate both Fβ and HM fitting and so acts to unify these models. All these approaches then assume that scattered light comes from only the intersection of the CME front with the Thomson sphere. Liu et al. (2016) compared estimations of CME kinematics resulting from the different assumed CME geometries (i.e., Fβ and HM). For Fβ techniques, at large observing angles, unphysical acceleration can arise, especially when the CME propagation direction is far away from the observer (Liu et al. 2013). HM geometry may overestimate the CME size near the Sun with a shape too simple to represent the real CME structure. Barnard et al. (2017) also analyzed the kinematics of four CMEs by applying three different technologies (HM, SSE, and ellipse evolution geometric models) and found that the discrepancies between the three technologies are smaller than the observational errors. CME front shapes are known to undergo significant distortion as they expand into the heliosphere, usually becoming flattened as a result of their interaction with the background solar wind (Owens et al. 2017). A detailed treatment of CME geometry must be performed in determining CME kinematics, especially for events with large longitudinal separation. On a J-map, CMEs appear as a bright feature with a positive gradient: multiple CME fronts seen in HI images appear as a bifurcation of features in a J-map. If only the front edge of the CME track in a J-map is considered, this can introduce significant errors into the predicted arrival time at Earth (Liu et al. 2016). In the ghost front model, we interpret the bifurcated structures in the J-map as the tangent part and nose part of a CME, and we consider this single front to evolve as a kinematically distorting flux rope (KDFR; Owens et al. 2006). A KDFR represents a physically constrained model that can be used to calculate the elongation angles of the flank and nose parts of a CME. Further, the part of the CME front intersecting Earth can be used to estimate the expected CME kinematics at Earth, including the arrival speed of the CME at Earth, which improves the forecast value of its geoeffectiveness (Owens et al. 2020b).

When describing a CME as a KDFR, three parameters need to be initialized: the half angle of the CME, the direction of propagation with respect to the observer, and the initial velocity of the CME. For the current analysis, which uses a drag model, an average solar wind speed needs to be defined, along with an empirical drag coefficient. The initial speed, position, half angle, and propagation direction of the CME were obtained by using the graduated cylindrical shell (GCS; Thernisien et al. 2006, 2009) model, in which the 3D shape of the CME can be iterated until a best match is obtained with coronagraph images. Having established the initial geometry of the CMEs, we use a drag function to describe the ICME deceleration through the inner heliosphere (Vršnak et al. 2001). The average background solar wind velocity was obtained from in situ observations of the ambient solar wind at 1 au.

Having determined the initial conditions for the CME, the expansion of the KDFR was calculated for a range of values of the empirical drag coefficient. The elongation of the nose and flank of the CME was estimated from this as a function of time, and these modeled values were compared with the observations by calculating the total residual between the model and observed elongation profiles for the CME nose. Subsequently, the width of the CME was adjusted to match the model to the observed elongation profile of the CME flank. Having determined the parameters that generated the best match between modeled and observed values, we used these to estimate the evolution of the longitudinal shape of the CME front. This in turn enabled the CME kinematics along the Sun–

Earth line and at the L1 point to be modeled for comparison with the in situ data. Constraining the model with observations in this way provides additional information about the longitudinal extent of the CME, which in turn will help with the interpretation of CME evolution, interaction, and (for events in which some portion of the front is Earth-directed) arrival time at Earth.

ICMEs, the heliospheric counterparts of CMEs, were originally identified by in situ observation. Chi et al. (2016) compiled an ICME catalog using the Wind spacecraft MAG and SWE data. According to different in situ signatures, all ICMEs are divided into three types: isolated ICMEs (I-ICMEs), multiple ICMEs (M-ICMEs), and shock-embedded ICMEs (S-ICMEs; Shen et al. 2017). If a slow CME and a fast CME successively erupt from the Sun at similar times and locations, the shock wave driven by the faster CME will catch up, interact with, and travel through the preceeding slow CME during their propagation in interplanetary space (Lugaz et al. 2009, 2017; Shen et al. 2017). ICMEs are usually restricted to single-point in situ observation in near-Earth space. In situ data from spacecraft situated in the inner heliosphere can be used to consolidate the CME prediction model, but this currently requires CMEs to occur during planetary alignments, and such events are rare. For example, Venus Express (VEX) is in a polar orbit around Venus, located at 0.72 au, and can provide observations of the heliospheric magnetic field (Zhang et al. 2006). On 2012 June 13–14, the longitude of Venus brought it within ∼5° of the Sun–Earth line. During this epoch, a series of CMEs erupted from a solar region located on the Earthward solar hemisphere. This sequence of events has been studied by several authors (for example, Srivastava et al. 2018; Kilpua et al. 2019; Scolini et al. 2019). Two Earth-directed CMEs erupted in quick succession and interacted with each other somewhere in the heliosphere ahead of their arrival at Earth.

We have also analyzed these events, considering each CME to be expanding as a KDFR into a uniform solar wind while being decelerated using a drag-based model, in Section 2. In addition, we constrained our technique by iterating the drag coefficient and CME width to minimize the difference between observed and modeled elongations of the CME flank and nose. As a consequence, the arrival times and CME speeds at both Earth and Venus were estimated for these two events, which are tested through comparison with in situ observations at Venus and Earth, respectively, in Section 3.

2. CME Remote Observations and Data Analysis

The two successive CME events analyzed in this study erupted between 13 and 14 June 2012. Both of the two CME events have wide-angle coverage from STEREO-A(STA)/B (STB) and in situ signatures at Wind and VEX in orbit around Venus. Images of the two CMEs were captured by Solar and Heliospheric Observatory (SOHO)/Large Angle and Spectrometric Coronagraph Experiment (LASCO) C2 as halo CMEs at 13:25 UT on 2012 June 13 and 14:12 UT on 2012 June 14 (subsequently referred to as CME-1 and CME-2 in this paper), as initially reported by Srivastava et al. (2018). Figure 1 (produced using the STEREO Science Center orbit tool) displays the positions of four widely separated spacecraft (Wind, VEX, STA, and STB) relative to the Earth and Sun in heliocentric Earth-ecliptic (HEE) coordinates on 2012 June 15 00:00 UT. At that time, STA and STB were 117° west and 118° east of the Earth with a distance of 0.96 au and 1.0 au from the Sun, respectively. The west-limb view from STB and east-limb view from STA indicate that the two CMEs are Earth-directed CMEs. Based on their appearance in coronagraph images, they are associated with the same active region NOAA 11504, accompanied by an M1.2 and M1.0 flare, respectively (see details in Srivastava et al. 2018). Venus and Earth were separated by ∼5° in heliospheric longitude (almost radially aligned) during the propagation of the two CMEs.

2.1. 3D Reconstruction in COR2 Field of View

The initial speeds, propagation directions, and half angles of the two CMEs were obtained from the coronagraph images. We used the stereoscopic observations from STEREO and SOHO with a GCS model to reconstruct the 3D geometry of the two successively erupting CMEs, as Hess & Zhang (2017) have done for Earth-affecting CMEs of Solar Cycle 24. This model involves taking a cylindrical croissant defined by six free parameters: longitude, latitude, tilt angle of axis, aspect ratio, half angle, and height. We apply the GCS model to contemporaneous images from STEREO/SECCHI/COR2-B, SOHO/LASCO, and SECCHI/COR2-A. The parameters were chosen such that the model image provides a good morphological approximation to the observed images from multiple viewpoints. The images of CME-1 and CME-2 overlaid with the fitted GCS wireframe contours are shown in Figure 2. The first row shows the appearance of CME-1 in the direct images from STB COR2 (left), SOHO C3 (middle), and STA COR2 (right) around 17:24 UT on 2012 June 13. At that time, the best visual GCS fitting shows that the propagation direction of CME-1 (height of 13.3 $R_{\odot}$) was 5° east, 30° south off the Sun–Earth line, and the half angle was 38°. The propagation direction and half angle of CME-1 are consistent with the results from Srivastava et al. (2018) and Kilpua et al. (2019). The true deprojected CME speed can be determined with a GCS model based on the 3D geometry. The CME velocities are based on linear fits to the leading-edge height measurements from the GCS model in the coronagraph data. The estimated fastest 3D velocity of CME-1 in COR2 was estimated to be $656.8 \pm 83\ \mathrm{km\ s^{-1}}$.

CME-2 first emerged into the FOV of STEREO/COR2 at around 14:09 UT on 2012 June 14, about 24 hr after the first appearance time of CME-1 in the same coronagraph. We also fitted the GCS model for CME-2 for the time around 15:39 UT by exploiting the concurrent image triplets of STA COR2, STB COR2, and SOHO C3, as shown in the second row of Figure 2. When the outlines of the GCS model matched the outer edges of CME-2 in all three views of white-light coronagraphs, the propagation longitude and latitude of CME-2 were found to be E2°, S25°, apparently an Earth-directed CME. The half angle of CME-2 is 28°, and the obtained fastest velocity of CME-2 in the FOV of COR2 is $1236.4 \pm 83\ \mathrm{km\ s^{-1}}$. The reconstructed latitude and longitude of the two CMEs suggest that they were Earth-directed and that CME-2 was traveling faster than CME-1. Even though the launch of CME-1 preceded that of CME-2 by approximately 24 hr, it was expected that these two CMEs would interact with each other in the inner heliosphere according to the directions and velocities of the two CMEs.

2.2. Reconstruction of CMEs in HI FOV

There is still a disagreement about when and where the two CMEs interacted with each other. Srivastava et al. (2018)

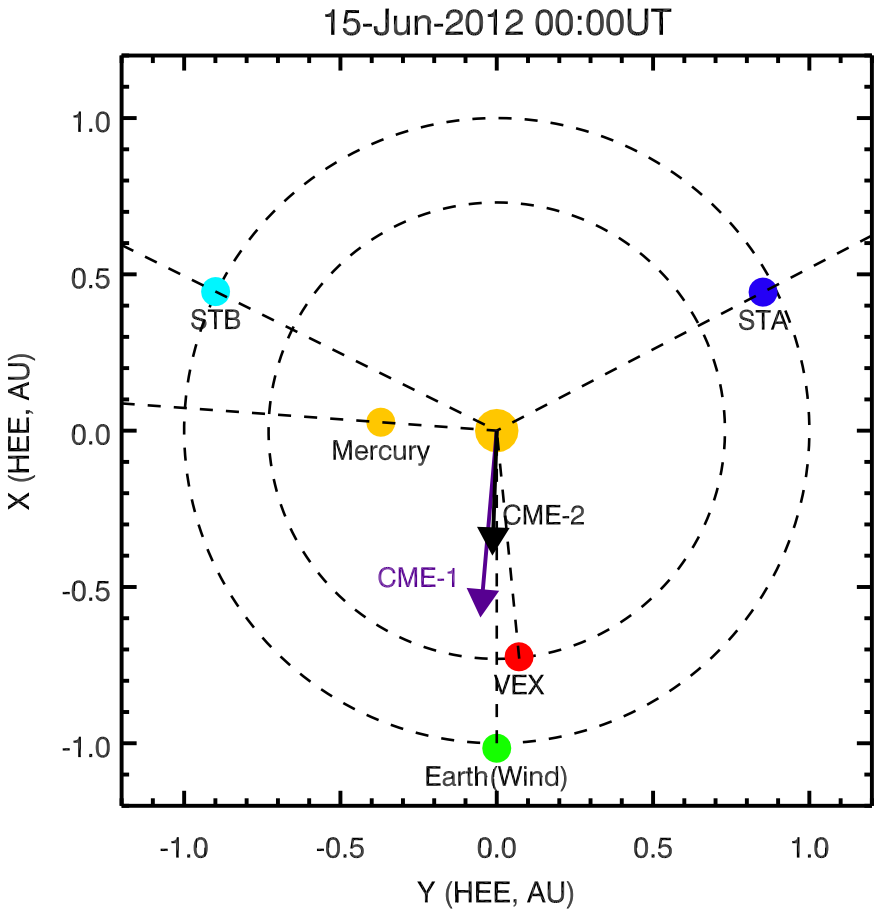

Figure 1. Positions of four separated spacecraft (Wind, VEX, STA, and STB) on 2012 June 15 00:00 UTC in the inner heliosphere. The purple and black arrows represent the reconstructed propagation directions of CME-1 and CME-2 from the GCS model, respectively.

proposed that the interaction occurred between 8:40 UT and 15:50 UT in a 7.2 hr span on 2012 June 15 at around 100 $R_{\odot}$ (∼0.47 au). In contrast, Kilpua et al. (2019) estimate a later interaction between the two CMEs at ∼0.72 au, after the orbit of Venus. Therefore, it is appropriate to apply new methods to provide further insight on how these CMEs propagate and interact with each other throughout the inner heliosphere.

2.2.1. Heliospheric Observations

As they propagated out from the Sun, CME-1 and CME-2 were clearly observed in the STEREO HI-1 cameras. These cameras have a 20° FOV, extending from 3° to 21° elongation from the Sun. CME-1 first appeared in the HI-1 FOV at 17:29 UT on 2012 June 13. The multiple ghost fronts of CME-1 are visible in the running difference images (in which two consecutive images are aligned and the difference taken in order to highlight moving features), as shown in Figure 3 panels (a, b). CME-2 also shows similar characteristics in HI-1 images (panels (c, d) of Figure 3). The initial propagation directions of the CMEs were found to be more than 100° from the Sun–STA/STB lines. For this geometry, the multiple fronts cannot be explained by multiple intersections between the CME front and the Thomson sphere. The VEX in situ observations do not show a clear fast-forward shock ahead of CME-1. Thus, here we interpret the outer and inner fronts observed by HI as the tangent and nose of CME-1, respectively. The velocity of CME-2 is much faster than the background solar wind. It is reasonable to believe that CME-2 was capable of driving a fast-forward shock ahead of it. This is also confirmed by in situ observations from Venus and Earth. Thus, the two fronts of CME-2 observed by HI could correspond to a buildup of plasma associated with the tangent and nose of the shock driven by CME-2.

To facilitate the comparison between imaging data and in situ observation, we only consider the fronts on the ecliptic. The green and red (yellow and white) dots in Figure 3 show the positions of the tangent and nose of CME-1 (CME-2) along the ecliptic. In this way, the propagation of the two CME fronts can be plotted as a function of elongation angle against time in a J-map (Sheeley et al. 1999, 2008), which is formed by taking slices along the ecliptic plane through the HI images and stacking them as a function of time (Davis et al. 2011). Figure 4 is a J-map of STA for 2012 June 13–18. J-maps are constructed using running difference images in order to enhance the faint propagating transient features and are shown in Figure 4 panel (a). According to the time of first appearance of the CMEs in COR2, we can easily associate bright curves in the J-map with the enhanced density structures of CME-1 and CME-2.

CME-1 and CME-2 are easily seen in SECCHI coronagraph images at low elongations, but they fade rapidly at large distances from the Sun, due to the expansion of the CMEs and the large angle between the CME propagation and observer. As shown in Figure 4 panel (a), the track of CME-1 became ambiguous when the elongation barely extends beyond 20° and cannot be observed in the outer HI-1 FOV from STA. The two fronts observed in HI-1A associated with CME-1

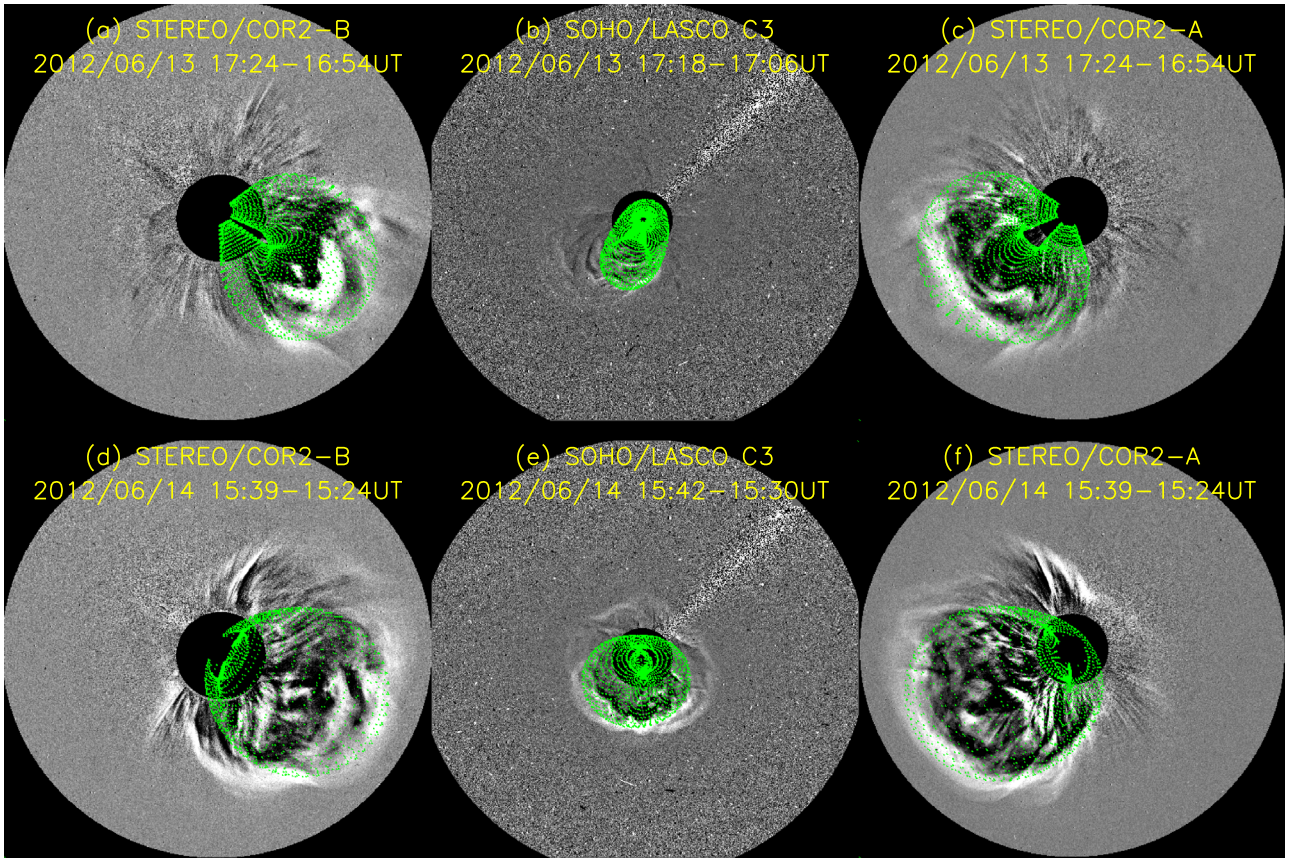

Figure 2. Contemporaneous image triplets for each of the CMEs observed from SECCHI/COR2-B (left), SOHO/LASCO (C3) (middle), and SECCHI/COR2-A (right) are shown with the GCS wireframe (green) overlaid on it. The panels show running difference images of CME-1 (top) between 17:18 and 17:24 UT on 2012 June 13, and of CME-2 (bottom) between 15:39 and 15:42 UT on 2012 June 14.

show a clear bifurcated structure in the J-map, with the elongation angle between the two fronts becoming larger as the CME propagates Earthward.

Even though CME-2 is also far from the Sun-STA line, it can be observed well into the STA HI-2 FOV, up to about 30° elongation (corresponding to the elongation of Earth). The brighter trace of CME-2 is likely associated with the piled-up mass of plasma, which has been compressed by interaction between the two CMEs. The two traces associated with CME-2 begin to bifurcate at a small elongation angle, less than 10°. The bifurcated structures observed in the J-map have been discussed by Liu et al. (2012) and Harrison et al. (2012). They explained the leading bifurcated feature as the shock wave and the trailing one as another structure after CME–CME interaction (Liu et al. 2012). In this work, we argue that the bifurcated structures of CME-1 and CME-2 are formed well before the interaction between the two CMEs, as shown in Figure 4 panel (a). No other CMEs were observed by wide-angle imaging observations during this time. Hence, we argue that the bifurcated structures correspond to the tangent and nose of the same CME structure, as explained by the ghost front model (Scott et al. 2019). The tracks associated with the two CMEs do not appear to merge or cross with each other in the J-map made with STA data.

2.2.2. Using Ghost Fronts to Estimate CME Kinematics and Arrival Times at Venus and Earth

The initial conditions of CME-1 and CME-2 (CME-1: propagation longitude with respect to Earth: E5°, half angle: 38°, speed: 656.8 km s^{-1}; CME-2: propagation longitude with respect to Earth: E0°, half angle: 28°, speed: 1236.4 km s^{-1}) were determined from the coronagraph data at 11.6 and 6.1 solar radii, respectively, using the GCS model. We assumed that beyond the FOV of COR2, CME-1 and CME-2 continued to propagate along the same direction; that is, we assumed that there was no heliospheric longitudinal deflection. The mean background solar wind velocity was obtained from Wind in situ observations at L1. By examining the radial solar wind speed at L1 for a period of 10 hr ahead of the CME arrival, the average background solar wind velocity was estimated to be 424.5 ± 23.5 km s^{-1}.

In order to compare the model with the data, we calculated the expansion of the CME as a KDFR being decelerated by the background solar wind, starting from the initial CME conditions determined from the coronagraph observations. The model was repeated for a range of drag coefficients, with the run producing the best match between the observed and modeled elongations of the CME nose being selected. For CME-1, the nose part of the CME time-elongation plot is best fitted using a drag parameter of 5.7×10^{-8} km^{-1}, as shown with the red dashed–dotted line in Figure 4. This value is within the recommended range (10^{-8}–10^{-7} km^{-1}) suggested by Vršnak et al. (2013). The time-elongation curve of the CME tangent is calculated automatically according to the width of the CME, as shown with the green dashed line in Figure 4. The CME half-width can be adjusted to improve this match, but as can be seen from the J-map of STA, the simulated green curve fitted the leading bifurcated feature of CME-1 well using the

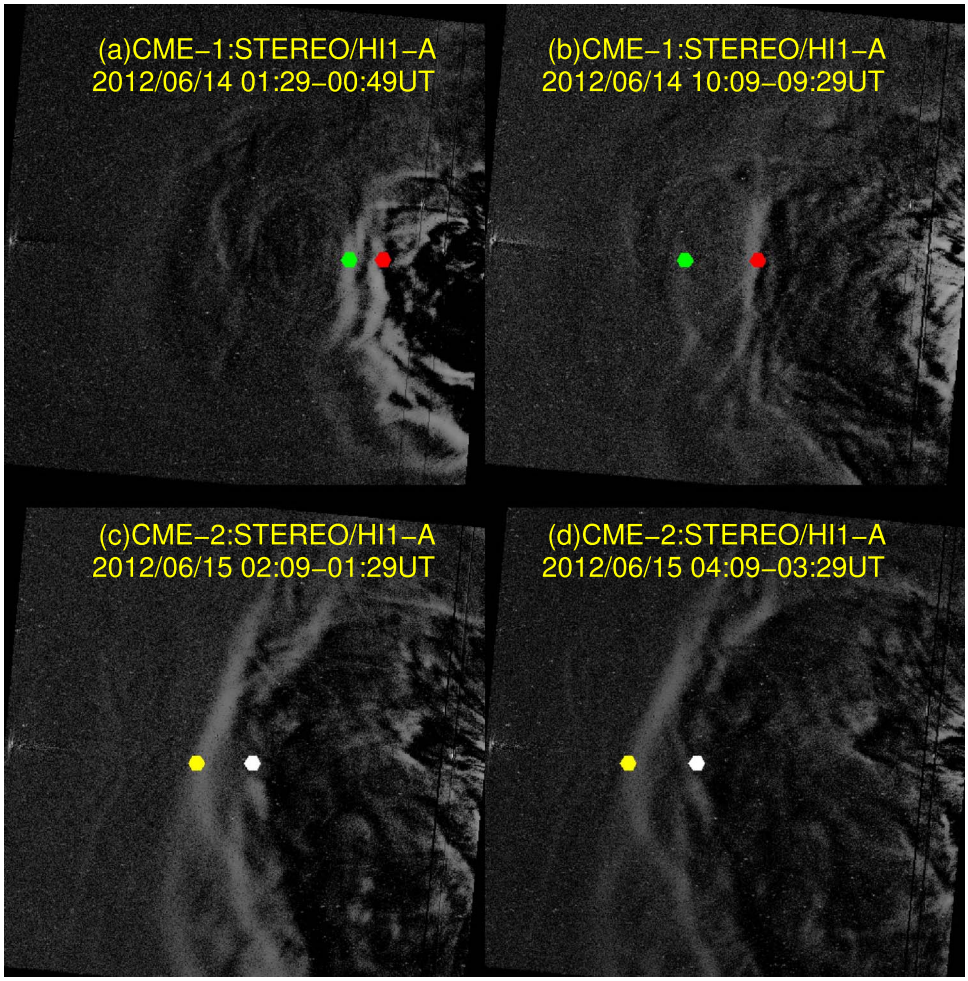

Figure 3. Four running difference images from STEREO/HI-1-A show (a) CME-1 at 01:29 on 2012 June 14, (b) CME-1 at 10:09 on 2012 June 14, (c) CME-2 at 02:09 on 2012 June 15, and (d) CME-2 at 04:09 on 2012 June 15. Two ghost fronts of CME-1 and CME-2 are visible. We interpret the outer and inner fronts as corresponding to the tangent and nose, respectively, of a single CME structure. The dots represent the position of multiple fronts along the ecliptic.

value of the half-width determined from the coronagraph data. The same analysis was conducted for the J-map from STB assuming the same width, propagation direction, initial velocity, and background solar wind. However, in the STB J-map, the two modeled fronts are consistently closer in elongation than the observations would suggest. The match to the flank of CME-1 is poor for the assumed width and propagation. As discussed in Scott et al. (2019), the differences between two spacecraft can be explained by deviations from a uniform background solar wind distorting the CME front.

According to the propagation directions of CME-1 and CME-2, one would expect VEX and Wind to encounter the part of the front between the nose and flank observed by STA. Therefore, in this manuscript we only consider the observations from STA. The black horizontal lines in Figure 4 show the elongation angle of the planets Venus and Earth, respectively. Venus is seen at the elongation angle of 29°.37. Using the best-fit drag coefficient and constant background solar wind for each CME, the derived speed at Venus is 491.1 km s^{-1}, and the estimated arrival time of CME-1 is 19:54 UT on June 15. At 1 au, the estimated arrival time of CME-1 is 21:54 UT on June 16, with a velocity of 473.5 km s^{-1}. Owens et al. (2017) suggest that CME arrival time forecasting is sensitive to the ambient solar wind structure. The errors of predicted arrival time and velocity are shown in Table 1, according to the observed range in background solar wind velocity.

A bifurcation in features within CME-2 is also observed in the STA J-map, as shown in Figure 4 panel (a). Having determined the time-elongation profile of CME-2 by manual tracking, we again used the initial CME observations to simulate the kinematics of CME-2 assuming it evolved as a KDFR. The white and yellow curves in Figure 4 panel (b) show the modeled elongation angles calculated for the nose and tangent of the CME-2. For this CME, the best match between the observed and modeled nose of CME-2 in the J-map was obtained for a drag parameter of 3.1×10^{-8} km^{-1}, which is comparable with the drag parameter (2.15×10^{-8}–3.15×10^{-8} km^{-1}) obtained from Kubicka et al. (2016) by constraining the arrival time of CME-2 at VEX. The drag parameter of CME-2 is significantly lower than that of CME-1, which is consistent with CME-1 clearing some of the ambient solar wind mass, resulting in a rarefied, perturbed solar wind ahead of CME-2 (Lugaz et al. 2005; Liu et al. 2014; Temmer & Nitta 2015; Temmer et al. 2017). The disturbed conditions for interplanetary space caused by CME-1 can last at least three days, which means CME-2 experiences less drag from the surrounding environment and could maintain a higher speed (Temmer et al. 2017). Again, the fit to the CME flank could be improved by iterating the CME width, but this

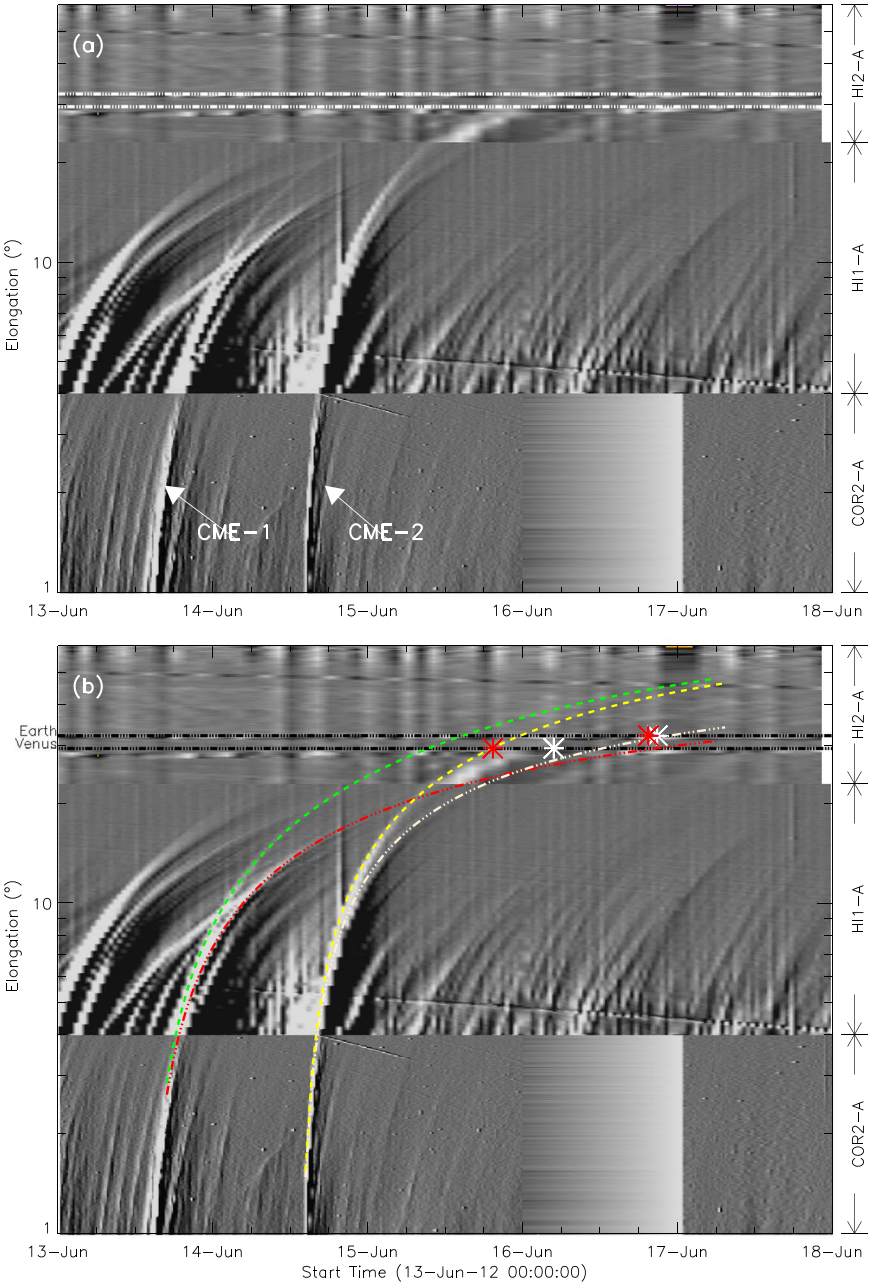

Figure 4. Time-elongation maps (J-maps) constructed from running difference images of COR2, HI-1, and HI-2 along the ecliptic plane for STA. Panel (a) shows the original J-map. Panel (b) shows the J-map with simulation results of CME-1 and CME-2. The tracks of the flank and nose of CME-1 in panel (b) are shown as green and red curves, respectively. The yellow and white curves show the fits to the tracks of the flank and nose of CME-2. The red and white asterisks indicate the arrival time of CME-1 and CME-2, respectively, at Earth and Venus, as determined from in situ spacecraft observations. The black horizontal dashed lines mark the elongation angles of Earth and Venus.

did not prove necessary for this event. The estimated speed of CME-2 at Venus is 636.0 km s^{-1} and the estimated speed at 1 au is 581.0 km s^{-1}. The estimated arrival time at Venus is 02:24 UT on 2012 June 16 and at Earth is 22:24 UT on 2012 June 16. As with CME-1, the estimated uncertainties in these results are shown in Table 1.

2.2.3. Interaction between CMEs

The simulated elongation angles of CME-1 and CME-2 intersect in Figure 4 panel (b), indicative of an interaction between these two CMEs (Liu et al. 2012). The elongation angle of a given feature in the J-map can be converted to heliocentric distance by reference to the evolving shape of the KDFR in the model. Figure 5 shows the simulated positions of the two CMEs at 16, 17, 18, and 19 hr from the launch of CME-2. In these figures, the red circle represents the Sun, the upper and lower triangles show the positions of STA and STB, respectively, and the cyan and magenta lines represent the outer boundaries of CME-1 and CME-2. In this simulation, we have considered the evolution of the two CMEs separately, ignoring the effect of interaction between the two CMEs on their velocity and direction. According to Figure 5, CME-2 starts to interact with CME-1 at about 17 hr after it was launched. At that time, both CMEs had yet to arrive at Venus. Thus, the two CMEs may appear as a shock-ICME structure in VEX in situ

Table 1
Predicted and Observed Arrival Times of CME-1 and CME-2

Target	Venus		Earth	
	CME-1	CME-2	CME-1	CME-2
Predicted arrival time (UT)	2012 Jun 15 19:54:00(+1/−0)	2012 Jun 16 02:24:00(+1/−0)	2012 Jun 16 21:54:00(+2/−1)	2012 Jun 16 22:24:00(+1/−1)
Observed arrival time (UT)	2012 Jun 15 19:24:00	2012 Jun 16 04:53:00	2012 Jun 16 19:30:34	2012 Jun 16 20:53:30
Predicted arrival speed (km s^{-1})	491.1 (+10.6/−15.9)	636.0 (+8.1/−14.7)	473.5 (+14.1/−18.2)	581.0 (+14.2/−16.0)
Observed arrival speed (km s^{-1})	…	…	473.0	527.2

observations. When CME-1 arrived at Earth, CME-2 had almost caught up with CME-1.

Many studies have shown that the interaction between CMEs can influence the speed and direction of those CMEs (Liu et al. 2012; Shen et al. 2012; Mishra et al. 2015a, 2015b). Thus, the interaction between CME-1 and CME-2 may affect their arrival time and velocity, which can be noted by in situ measurements (Burlaga et al. 2002). In order to investigate the effect of the CME–CME interaction, we next use in situ observations from Wind and VEX to obtain the arrival time and velocity of these two ICMEs and compare them with the simulated results.

3. Comparing Remote and In Situ Observations to Determine CME Kinematics

During the passage of the CMEs, Earth and Venus were almost radially aligned. This means that in situ measurements are available from spacecraft in orbit around both Venus and Earth. Although observations of CMEs by the STEREO HI instruments arriving at Venus (Rouillard et al. 2009) and Earth (Davis et al. 2009) are relatively common, events when the alignment of Earth and Venus is close enough for them to be seen at both locations are rare. The angle in HEE longitude between Earth and Venus was 5.°4; to simplify the analysis, we neglect this small separation angle between them. According to the propagation direction of the two CMEs determined from the coronagraph observations, the two CMEs intersected both Venus and Earth. This is one of the closest radial conjunction events of Venus with Earth during which Earth-directed CMEs were observed. Although the CME first impacted VEX before impacting Wind, we describe the Wind in situ measurements first, as the availability of plasma measurements makes it easier to identify the start and end times of the CME substructures.

Figure 6 shows 1-min averaged in situ measurements taken by the Wind spacecraft from 2012 June 16 to June 18, together with the 1 hr Dst index measured by ground-based magnetometers at Earth (provided by the World Data Center for Geomagnetism, Kyoto; http://wdc.kugi.kyoto-u.ac.jp/dstdir/). At 19:30 UT on June 16, the first fast-forward shock impacted Wind (hereafter S1, represented by the yellow vertical line in Figure 6), characterized by a sudden enhancement in magnetic field intensity and solar wind velocity. According to the IPshocks.fi database of Kilpua et al. (2015), the magnetic field compression ratio of S1 is 1.87. The shock driven by CME-1 is the most likely source of S1, as the estimated arrival time of CME-1 is only two hours later than S1. One and one-half hours after the arrival of S1, the second shock (hereafter S2) was observed at 20:53 UT on June 16, with a magnetic field compression ratio of 1.58. S2 is likely associated with the shock driven by CME-2. The huge increase in density after S2 indicates a pile-up or compression of the plasma as the shock passes through the magnetic cloud. The dense sheath lasts about 1.5 hr. From 22:07 UT 2012 June 16 to 11:20 UT 2012 June 17 (yellow shaded band in Figure 6, E1), the in situ observations show a typical ICME structure, with enhanced magnetic field intensity, declining velocity profile, low proton temperature, and low plasma β. This ICME is listed in the database of Chi et al. (2016) and Richardson & Cane (2010). While the shocks are usually unambiguous in arrival, the ejecta arrival time is more subjective, especially for complex interacting events such as this (Hess & Zhang 2015). Kilpua et al. (2019) marked the first 1.5 hr of E1 as the flux rope related to CME-1, and the trailing part (10.5 hr) of E1 as the flux rope associated with CME-2. They also found an associated structure in VEX in situ observations to explain that CME-1 and CME-2 had not interacted with each other when they arrived at Venus. In this paper, we prefer the interpretation that E1 is associated with CME-1. We have at least two reasons: (1) The in situ parameters of E1 changed smoothly. No obvious observational signatures of an interacting region can be observed in the duration of E1, such as the magnetic field becoming less regular and its strength clearly decreasing, and the beta value increasing to a high level in the interacting region (Wang et al. 2003). (2) Another ICME structure can be recognized from 20:02 UT June 17 to 04:23 UT June 18, which may be associated with CME-2. This ICME is marked by the green shaded area in Figure 6 (E2), where the in situ observation shows an enhanced total magnetic field intensity, a smoothly changing direction of the magnetic field, and low plasma β. The enhanced magnetic field and density of E1 indicated the compression of S2 on E1. Even though the shock (S2) propagates through E1, the dense sheath behind the shock must remain between the two magnetic ejecta (Lugaz et al. 2008, 2017). The region between E1 and E2 shows a period of weaker and more turbulent magnetic field, abnormally large plasma β, and hotter plasma temperature, which may be an indication of compression between the ejecta (Wang et al. 2003). The negative z-component of the magnetic field in the trailing part of E1 triggered the beginning of a geomagnetic disturbance, marked by a decrease in the Dst index to about −71 nT. The shock compression may have enhanced the intensity of the geomagnetic storm (Shen et al. 2017, 2018; Xu et al. 2019).

For VEX, there is no high-resolution plasma data available. Figure 7 shows the magnetic field measured by VEX/MAG (Zhang et al. 2006). The x, y, and z components of the magnetic field are given in Venus Solar Orbital (VSO) coordinates. The yellow shaded region (E1) indicates the interval of an ICME

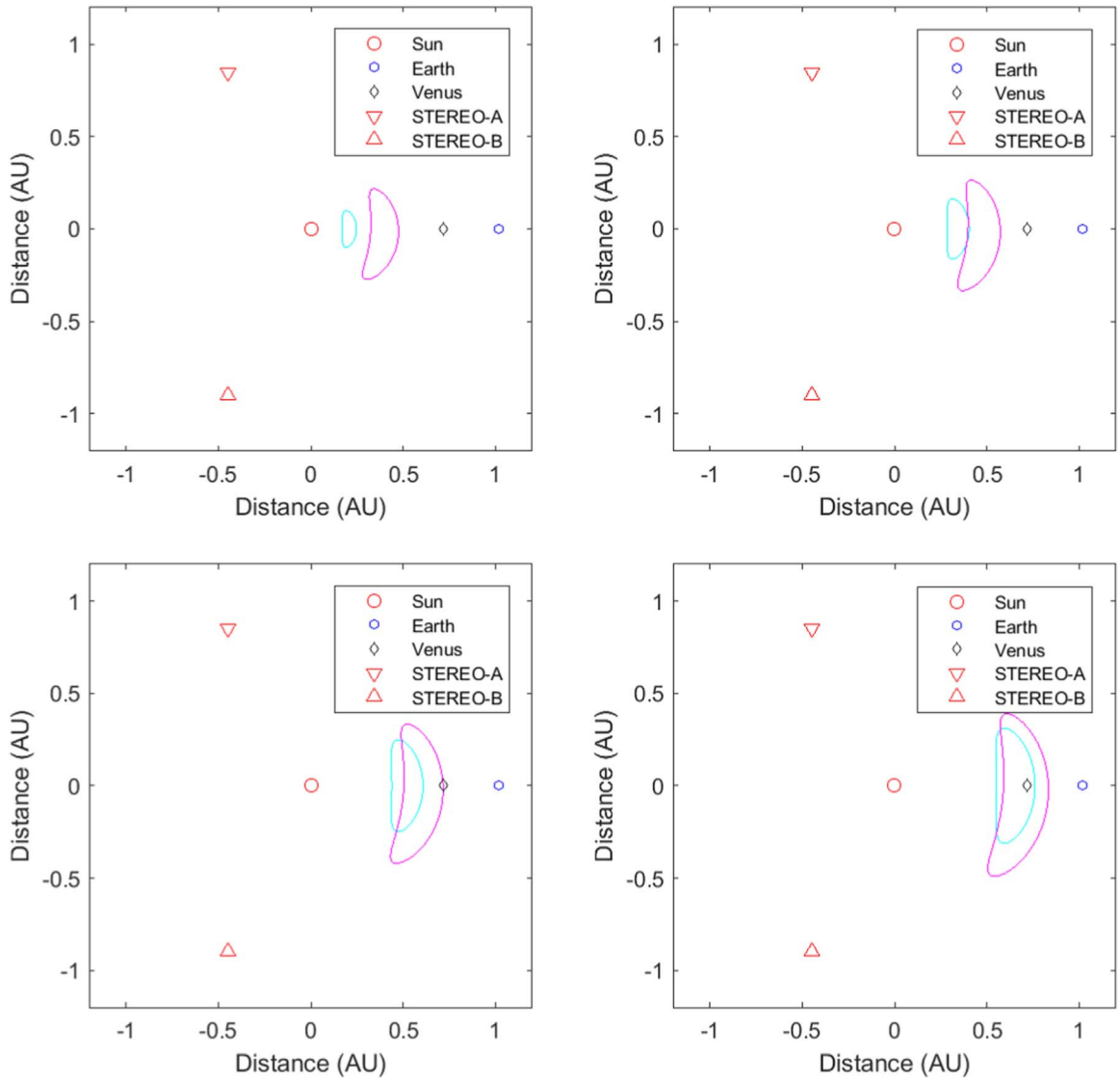

Figure 5. Simulated positions in the ecliptic plane of CME-1 and CME-2 at different times in the simulation. The magenta and cyan lines show the positions of CME-1 and CME-2, respectively. The red and blue circles show the positions of the Sun and Earth, the blue diamond shows the position of Venus, and the upper and lower triangles indicate the positions of STEREO A and B.

(∼13 hr from 19:24 UT June 15 to 08:30 UT June 16), which is in the database of ICMEs measured at Venus by VEX (Good & Forsyth 2016). E1 is most likely associated with CME-1 and is about half an hour earlier than the estimated arrival time of CME-1, identified by a relatively smooth rotation of the magnetic field direction consistent with a flux rope structure, coinciding with a relatively enhanced magnetic field strength. The duration of E1 at Venus was not significantly different from that at Earth. Janvier et al. (2019) studied the average ICME duration increase from Venus to Earth's orbits and found that the typical ejecta duration increases by a factor of 1.3. This indicates that in this case, E1 was likely compressed by the shock or other structures during its propagation from Venus to Earth. At the trailing part of E1, the ejecta was characterized by the presence of an interplanetary shock (S2). Comparing with Wind in situ observations, we interpret this sudden jump of magnetic field as the shock driven by CME-2, which arrives at 04:53 UT June 16 (green vertical line in Figure 7). The two figures (Figures 6 and 7) show that the magnetic field strength profile (before the arrival time of S2) observed by VEX is qualitatively similar to the profile at Wind. The magnetic field intensity of E1 is higher at the CME leading edge than the center, which may be due to interaction between the CME leading edge and the ambient solar wind (Owens et al. 2017). The shock compressed the magnetic field of E1, resulting in a significant amplification of the magnetic field from a preexisting value of ∼40 nT to more than 70 nT. The magnetic field compression ratio of S2 is 1.74, a little larger than that observed at Earth. S2 was followed by a prolonged sheath region (with a duration of ∼14 hr) characterized by a fluctuating magnetic field. After that, a second period of enhanced magnetic field and smoothly changing magnetic direction was observed between 18:05 UT June 16 and 01:05 UT June 17. The green shaded region in Figure 7 shows its duration (E2). Compared with the in situ observation from Wind, the magnetic field strength profile of E2 did not change much between these observations. E2 is most probably associated with the CME-2 ejecta.

The in situ observations at Venus show a clear signature of a shock–ICME interaction event. It confirms the result that the

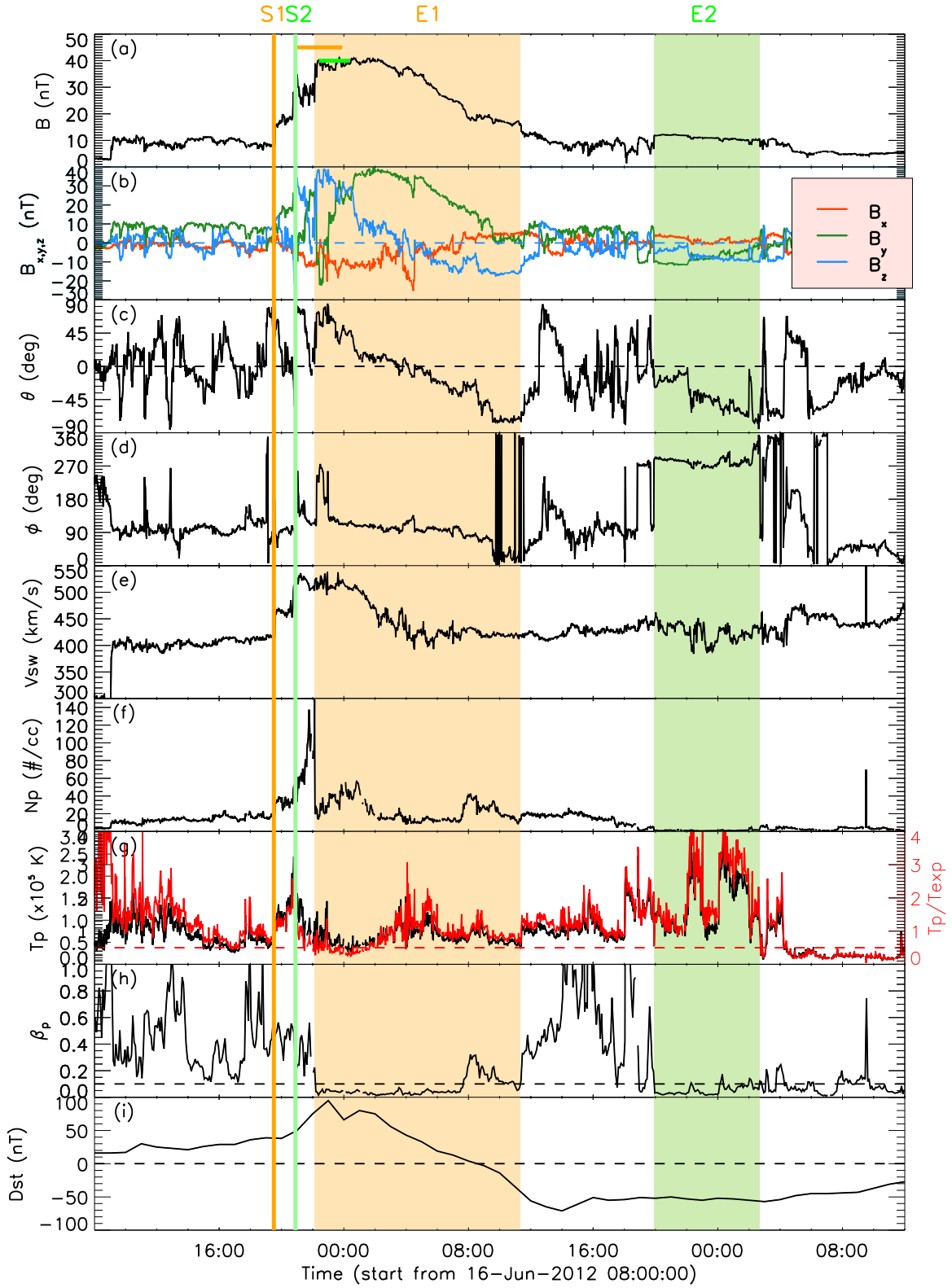

Figure 6. CME measurements at Wind. The panels show from top to bottom (a) the magnetic field strength; (b) the x, y, and z magnetic field components in GCS; (c, d) the elevation θ and azimuth ϕ of field direction in GSE; (e) the solar wind velocity; (f) the proton density; (g) temperature (red, expected temperature from Lopez 1987); (h) proton β; and (i) D_{st} index. The yellow and green vertical lines indicate the arrival of S1 and S2, respectively. The yellow and green shaded regions indicate the intervals of CME-1 and CME-2.

two CMEs interacted before CME-1 arrived at Venus. At Earth, the Wind in situ observations show that the shock driven by CME-2 had passed through the whole ejecta part of CME-1. The bright curved features observed in the J-maps correspond to Thomson scattering from higher density regions of plasma or those aligned along the observer's line of sight. Previous research has shown that the traces in the J-map correspond to the high-density region in the ICME sheath, which is usually at

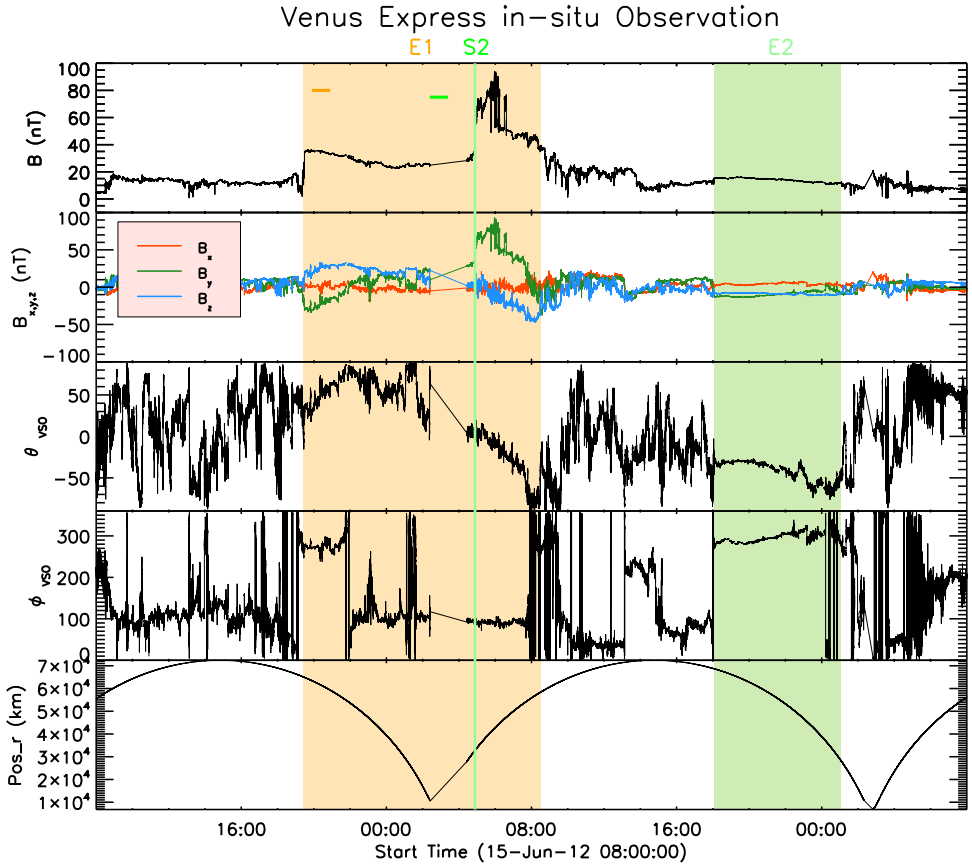

Figure 7. CME measurements at Venus. The panels show from top to bottom the magnetic field strength; the x, y, and z components in VSO coordinates; the elevation θ and azimuth ϕ of the magnetic field direction in VSO coordinates; and the radial distance of the spacecraft to the center of Venus. The green line indicates the S2 shock arrival. The yellow and green shaded regions indicate the intervals of CME-1 and CME-2.

the location of the shock (Liu et al. 2011; Möstl et al. 2014). At Venus, no high-resolution plasma data are available. Thus, we use the arrival time of the shock or leading edge of an ICME to indicate the arrival time of an ICME. Comparing the track in the J-map with VEX in situ observations, we find that the arrival times of E1 and S2 (the red and white asterisks in Figure 4 panel (b)) are located between the nose and flank parts of CME-1 and CME-2 at the elongation of Venus. No clear shock had formed ahead of CME-1 at the time it passed by Venus, according to VEX in situ observations. Hence, it is highly likely that for this CME event the two ghost fronts observed in the HI camera correspond to the different parts of the CME-1 ejecta. According to the KDFR model, the estimated arrival times of CME-1 and CME-2 at Venus are 19:54 UT on June 15 and 02:24 UT on June 16 (the yellow and green horizontal lines in Figure 7), respectively. The estimated arrival times agree with the in situ observations, within differences of 2.5 hr. At Earth, the high-density region of CME-1 corresponds to the location of S1. As shown in Table 1, the observed arrival time of CME-1 is about two and one-half hours earlier than the predicted arrival time. At the sheath region of CME-2, a density-enhanced region (the highest density value more than 140#/cc) is obtained at 21:51 June 16, about one hour later than the arrival of S2. The predicted arrival time of CME-2 at Earth is about two and one-half hours after the observation time of S2. As shown in Figure 6, the estimated arrival time of CME-2 is consistent with the density-enhanced region observed by Wind in situ measurements. At Earth, the predicted velocities of CME-1 and CME-2 are about 473.5 km s^{-1} and 566.7 km s^{-1}, respectively. All of the error bars of the predicted velocity are shown in Table 1. The estimated arrival velocities are again well confirmed by the in situ observation. The ghost front model is remarkable in giving the longitudinal information of CMEs and predicting the arrival time and velocity of CMEs. The differences between the estimated arrival time of CME-1/2 and the observation of E1 and S2 may be consistent with the interaction between two CMEs.

4. Discussion and Conclusion

We have investigated the kinematics of two CMEs launched on 2012 June 13–14, based on white-light remote-sensing and in situ observations from STEREO, SOHO, Wind, and VEX. Using the GCS model to estimate the initial CME conditions, we estimated each CME's expansion into the heliosphere by considering the CME outer boundary to be a KDFR expanding into, and undergoing drag deceleration from, a uniform solar wind (the latter having been determined from the in situ time series of solar wind data at L1). The duplicate "ghost" front seen in HI images has been interpreted as the nose of the CME, while the leading edge was considered to map to the CME flank, as suggested by Scott et al. (2019). Drag parameters were chosen that minimized the difference between the observed and modeled elongations of these fronts. The drag coefficient for CME-1 was significantly greater than for CME-2, consistent with the initial CME leaving a lower density solar wind in its wake into which CME-2 was propagating. As a result, it was

Table 2
Errors in Predicted Arrival Time and Velocity of CME-1 and CME-2 Based on Different Initial Parameters from GCS Model

Initial Time (UT)	Lon (deg)	Half Angle (deg)	Height ($R_\odot$)	Initial Speed (km s^{-1})	Error in Predicted Arrival Time (UT)	Error in Predicted Arrival Speed (km s^{-1})	Residual of Nose (deg)	Residual of Flank (deg)
CME-1:								
2012 Jun 13[b] 17:54	−20	26	15	719	V: −8.5[a] E: −14.6	V: — E: 194	1.93	0.94
2012 Jun 13[c] 16:54	−15	22.5	10.9	560	V: 1.5 E: 0.4	V: — E: 63	1.86	2.33
2012 Jun 13[d] 19:54	−10	38.6	21.5	657	V: −7.5 E: −12.6	V: — E: 170	0.46	0.29
2012 Jun 13[e] 18:24	−5	38	16.2	605	V: −2 E: −2.1	V: — E: 47	0.25	0.33
2012 Jun 13[f] 16:54	−5	38	11.6	657	V: 0.5 E: 2.4	V:— E: 0.5	0.16	0.2
CME-2:								
2012 Jun 14[b] 15:54	−5	40	15.2	1213	V: −4.5 E: −6.0	V: — E: 149	0.17	0.97
2012 Jun 14[c] 15:39	−2	30	13.5	900	V: −3.75 E: −8.2	V: — E: 342	0.74	0.89
2012 Jun 14[d] 17:18	−5	57	21.5	966.3	V: −6.1 E: −11.6	V:— E: 402	0.8	0.75
2012 Jun 14[e] 15:39	−4	28	13.4	1154	V: −4.75 E: −6.2	V:— E: 172	0.2	0.42
2012 Jun 14[f] 14:24	0	28	6.1	1236	V: 0 E: 1.5	V:— E: 54	0.14	0.18

Notes. Positive (negative) errors in predicted arrival time correspond to a predicted arrival time that is after (before) the actual CME arrival time determined from in situ measurements (VEX and Wind). Positive errors in predicted speed correspond to a predicted speed that is more than the actual CME speed at L1.
[a] V means VEX, and E means Earth.
[b] Initial parameters of CMEs are from Scolini et al. (2019).
[c] Initial parameters of CMEs are from Srivastava et al. (2018).
[d] Initial parameters of CMEs are from Kilpua et al. (2019).
[e] Initial parameters of CMEs are from our work: the last observation by the coronagraphs.
[f] Initial parameters of CMEs are from our work: the time of the estimated fastest velocity.

possible to model the propagation of these CMEs through the inner heliosphere, determine when they were most likely to interact, and make estimates of their arrival times at Earth and Venus.

The analysis of the two events confirmed that the bifurcated features in the J-map are consistent in elongation with the locations of the CME nose and tangent point to the flank. For the observation geometry during this event, the trailing bifurcated structure corresponded to the nose of the CME, and the leading J-map structure corresponded to the tangent point to the flank of the CME. The separation elongation angle between the bifurcated features is a function of CME width, shape, speed, and direction and, for this event, approximates the evolution of a KDFR expanding into a uniform solar wind.

Having constrained the estimated CME propagation by matching the observed and modeled fronts in this way, it was then possible to estimate the arrival time and velocity of each CME as it passed Venus and Earth. At Venus, the shock driven by CME-2 caught up with CME-1, showing a typical shock-ICME structure. According to observations from the Wind spacecraft, the shock driven by CME-2 had passed through CME-1 before arrival at Earth. By comparing the estimated and observed arrival times of each CME, our approach resulted in arrival time estimates within 2.5 hr of those observed at VEX and Wind. The longitudinal structure of the CMEs obtained by this approach has the potential to improve space weather forecasting. The accuracy of arrival times can be affected by uncertainties in the CME initial conditions, interaction between CMEs, distortion of the CME shape by solar wind structure, the presence of shocks, and the efficiency of solar wind drag on each CME. The relative importance of each such factor could be investigated through an ensemble approach. The drag-based ensemble model developed by Dumbović et al. (2018) is a possible option, but the method is not valid for CME–CME interaction events. In order to test the sensitivity of CME propagation direction and width to the predicted arrival time and velocity, we summarize the CME initial parameters from Srivastava et al. (2018), Kilpua et al. (2019), and Scolini et al. (2019) and two conditions from ours (the time at which the fastest velocity was estimated and the last observation by the coronagraphs). Table 2 shows the initial parameters from those studies and the errors in predicted velocity and arrival time. Note that the minimum value of the drag parameters we used here is 1×10^{-9} km s^{-1}, which was revealed as the lowest possible value (Rollett et al. 2014, 2016; Temmer & Nitta 2015; Kubicka et al. 2016). Based on that, there may exist a residual between the predicted profile and the observations. The residual values of nose and ghost fronts are shown in the last two columns of Table 2. For an Earth-directed CME, the residual between model and observed elongations of the CME nose will reflect the accuracy of the predicted arrival time and in situ velocity of the CME at Earth. The residual value between model and observed elongations of the CME flank provides information about how well the model reproduces the shape of the CME front, which is important for predicting the time and in situ speed at Earth for those CMEs whose flank

encounters the Earth. The model with the smallest residual values between model and observed elongations for both CME nose and flank provides the most creditable estimate of the in situ CME parameters at Earth, suggesting that the use of this technique can add to our forecast skill. In our analysis, the CME initial parameters estimated using the time and location of the fastest CME velocity observed in the coronagraph data produced the smallest residual between subsequent observed and model CME elongations. This should therefore be considered to be the best estimate of CME kinematics, and, if we were doing a weighted ensemble, this would be given a much higher weighting than the other runs. It should be noted that many of the other runs did not produce a minimum residual within the likely range of drag parameters, indicating that these runs are somehow not capturing the physics. Table 2 shows that different initial parameters change the predicted arrival time of CME-1 at Venus by 8.5 hr and at Earth by 14.6 hr in total. For CME-2, the prediction errors are found as 6 hr at Venus and 8 hr at Earth. The prediction errors are comparable to the mean absolute error obtained from the drag-based ensemble model (Dumbović et al. 2018). In future work, we will try to use the heliospheric upwind extrapolation model in large ensembles to efficiently investigate the effect on the CME transit time of the uncertainty in the initial CME parameters and ambient solar wind (Owens et al. 2020a). Our results indicate that CME-1 and CME-2 interacted with each other before they arrived at Venus, according to the propagation distances derived from our modeling. The in situ observation from Venus shows a typical shock-ICME complex structure, which provides confirmation of this interpretation. Our results also suggest that a CME–CME interaction is possibly involved in disrupting the propagation direction or geometry of each CME. Such a deflection and interaction is consistent with the fact that CME-1 (CME-2) reached VEX earlier (later) than expected (Shen et al. 2012, 2014; Wang et al. 2014, 2016). The difference between expected arrival time and observational arrival time is larger at Earth than at Venus. This implies that the interaction persisted between Venus and Earth.

In this work, we use the "ghost front" model to explain the multiple fronts of CMEs observed in the HI FOV and predict the arrival time of CMEs at VEX and Wind. Even though we get good predicted results compared to the observed arrival time, we should not rule out other possible explanations. Möstl et al. (2009) identified a similar double-front CME event, with the compressed front as its outermost edge and the dense material trailing as the following. The two bright features tracked from the Sun to STEREO-B were clearly identified in situ as two higher density regions bounding a magnetic flux rope. Further work, studying this event by including any other possible explanations for the double-front CMEs, is needed to advance our understanding of the multiple fronts seen in HI observations.

We must be aware of the limitations of this method. This model assumes that the background solar wind is uniform and that the CME propagates along a fixed radial trajectory, ignoring heliospheric deflection. In reality, the interaction between a CME and the background solar wind can distort the shape of the CME front, and the background solar wind velocity is reduced closer to the Sun (Riley & Lionello 2011). This may explain the differences in observations between the STA and STB. The preconditioning of the interplanetary space is also very important for CME propagation, CME kinematics, and space weather forecasting, especially for successively erupting CMEs (Temmer & Nitta 2015). Temmer et al. (2017) found that the disturbed conditions of interplanetary space by previous CMEs can last three to six days, which may affect the propagation behavior of the subsequent CMEs. In future work, we will consider the impact of a structured background solar wind (Lang & Owens 2019) and the preconditioning of interplanetary space in addition to the ghost front technique to determine their impact on CME kinematics and estimates of arrival time at Earth.

The authors are grateful to the referee for many helpful comments. We acknowledge the use of data from the SOHO, STEREO, and Wind spacecraft. STEREO is the third mission in NASA's Solar Terrestrial Probes program. We thank the STEREO HI team at the Rutherford Appleton Laboratory and the UK Solar System Data Centre for supplying the Heliospheric Imager data used in this study. SOHO is a project of international cooperation between the ESA and NASA. This work is supported by grants from the Strategic Priority Program of CAS (XDB41030100), NSFC (grant Nos. 41904151, 41822405, 41774181), Anhui Provincial Natural Science Foundation (1908085MD107), a project funded by the China Postdoctoral Science Foundation (2019M652194), and the Fundamental Research Funds for the Central Universities (WK2080000122). Y.C. acknowledges the support from the China Scholarship Council (CSC) under file No. 201906345002. We thank Luke Barnard for helpful discussions.

ORCID iDs

Yutian Chi https://orcid.org/0000-0001-9315-4487
Christopher Scott https://orcid.org/0000-0001-6411-5649
Mathew Owens https://orcid.org/0000-0003-2061-2453
Jie Zhang https://orcid.org/0000-0003-0951-2486
Yuming Wang https://orcid.org/0000-0002-8887-3919
Mike Lockwood https://orcid.org/0000-0002-7397-2172

References

Barnard, L. A., de Koning, C. A., Scott, C. J., et al. 2017, SpWea, 15, 782
Burlaga, L. F., Plunkett, S. P., & St. Cyr, O. C. 2002, JGRA, 107, 1266
Chi, Y., Shen, C., Wang, Y., et al. 2016, SoPh, 291, 2419
Davies, J., Harrison, R., Perry, C., et al. 2012, ApJ, 750, 23
Davis, C. J., Davies, J., Lockwood, M., et al. 2009, GeoRL, 36, L08102
Davis, C. J., de Koning, C., Davies, J., et al. 2011, SpWea, 9, S01005
Dumbović, M., Čalogović, J., Vršnak, B., et al. 2018, ApJ, 854, 180
Eastwood, J., Biffis, E., Hapgood, M., et al. 2017, Risk Analysis, 37, 206
Eyles, C., Harrison, R., Davis, C., et al. 2009, SoPh, 254, 387
Good, S., & Forsyth, R. 2016, SoPh, 291, 239
Gosling, J., McComas, D., Phillips, J., & Bame, S. 1991, JGR, 96, 7831
Harrison, R., Davies, J., Möstl, C., et al. 2012, ApJ, 750, 45
Hess, P., & Zhang, J. 2014, ApJ, 792, 49
Hess, P., & Zhang, J. 2015, ApJ, 812, 144
Hess, P., & Zhang, J. 2017, SoPh, 292, 80
Howard, R. A., Moses, J., Vourlidas, A., et al. 2008, SSRv, 136, 67
Janvier, M., Winslow, R. M., Good, S., et al. 2019, JGRA, 124, 812
Kaiser, M. L., Kucera, T., Davila, J., et al. 2008, SSRv, 136, 5
Kilpua, E., Lumme, E., Andreeova, K., Isavnin, A., & Koskinen, H. 2015, JGRA, 120, 4112
Kilpua, E. K. J., Good, S., Palmerio, E., et al. 2019, FrASS, 6, 50
Kubicka, M., Möstl, C., Amerstorfer, T., et al. 2016, ApJ, 833, 255
Lang, M., & Owens, M. J. 2019, SpWea, 17, 59
Li, X., Wang, Y., Liu, R., et al. 2018, JGRA, 123, 7257
Liu, Y., Luhmann, J. G., Bale, S. D., & Lin, R. P. 2011, ApJ, 734, 84
Liu, Y., Thernisien, A., Luhmann, J. G., et al. 2010, ApJ, 722, 1762
Liu, Y. D., Hu, H., Wang, C., et al. 2016, ApJS, 222, 23

Liu, Y. D., Luhmann, J. G., Kajdič, P., et al. 2014, NatCo, 5, 3481
Liu, Y. D., Luhmann, J. G., Lugaz, N., et al. 2013, ApJ, 769, 45
Liu, Y. D., Luhmann, J. G., Möstl, C., et al. 2012, ApJL, 746, L15
Lopez, R. 1987, JGR, 92, 11189
Lugaz, N., Farrugia, C., Davies, J., et al. 2012, ApJ, 759, 68
Lugaz, N., Manchester, W., IV., & Gombosi, T. 2005, ApJ, 634, 651
Lugaz, N., Temmer, M., Wang, Y., & Farrugia, C. J. 2017, SoPh, 292, 64
Lugaz, N., Vourlidas, A., Roussev, I., et al. 2008, ApJL, 684, L111
Lugaz, N., Vourlidas, A., & Roussev, I. 2009, AnGeo, 27, 3479
Maloney, S. A., & Gallagher, P. T. 2011, ApJL, 736, L5
Manchester, W. B., IV., Vourlidas, A., Tóth, G., et al. 2008, ApJ, 684, 1448
Mishra, W., Srivastava, N., & Chakrabarty, D. 2015a, SoPh, 290, 527
Mishra, W., Srivastava, N., & Singh, T. 2015b, JGRA, 120, 10221
Morrill, J., Howard, R., Vourlidas, A., Webb, D., & Kunkel, V. 2009, SoPh, 259, 179
Möstl, C., Amla, K., Hall, J. R., et al. 2014, ApJ, 787, 119
Möstl, C., Farrugia, C. J., Temmer, M., et al. 2009, ApJL, 705, L180
Owens, M., Lang, M., Barnard, L., et al. 2020a, SoPh, 295, 43
Owens, M., Lockwood, M., & Barnard, L. 2017, NatSR, 7, 1
Owens, M., Lockwood, M., & Barnard, L. 2020b, SpWea, 0, e2020SW002507
Owens, M. J., Merkin, V., & Riley, P. 2006, JGRA, 111, A03104
Poomvises, W., Gopalswamy, N., Yashiro, S., Kwon, R.-Y., & Olmedo, O. 2012, ApJ, 758, 118
Richardson, I. G., & Cane, H. V. 2010, SoPh, 264, 189
Richardson, I. G., & Cane, H. V. 2012, JSWSC, 2, A01
Riley, P., & Lionello, R. 2011, SoPh, 270, 575
Rollett, T., Möstl, C., Isavnin, A., et al. 2016, ApJ, 824, 131
Rollett, T., Möstl, C., Temmer, M., et al. 2014, ApJL, 790, L6
Rouillard, A., Davies, J., Forsyth, R., et al. 2009, JGRA, 114, A07106
Scolini, C., Rodriguez, L., Mierla, M., Pomoell, J., & Poedts, S. 2019, A&A, 626, A122
Scott, C., Owens, M., de Koning, C., et al. 2019, SpWea, 17, 539
Sheeley, N. R., Herbst, A., Palatchi, C., et al. 2008, ApJ, 675, 853
Sheeley, N. R., & Rouillard, A. 2010, ApJ, 715, 300
Sheeley, N. R., Walters, J., Wang, Y.-M., & Howard, R. 1999, JGRA, 104, 24739
Shen, C., Chi, Y., Wang, Y., Xu, M., & Wang, S. 2017, JGRA, 122, 5931
Shen, C., Wang, Y., Pan, Z., et al. 2014, JGRA, 119, 5107
Shen, C., Wang, Y., Wang, S., et al. 2012, NatPh, 8, 923
Shen, C., Xu, M., Wang, Y., Chi, Y., & Luo, B. 2018, ApJ, 861, 28
Srivastava, N., Mishra, W., & Chakrabarty, D. 2018, SoPh, 293, 5
Temmer, M., & Nitta, N. 2015, SoPh, 290, 919
Temmer, M., Reiss, M. A., Nikolic, L., Hofmeister, S. J., & Veronig, A. M. 2017, ApJ, 835, 141
Thernisien, A., Howard, R., & Vourlidas, A. 2006, ApJ, 652, 763
Thernisien, A., Vourlidas, A., & Howard, R. 2009, SoPh, 256, 111
Vourlidas, A., & Howard, R. A. 2006, ApJ, 642, 1216
Vršnak, B., Magdalenić, J., & Aurass, H. 2001, SoPh, 202, 319
Vršnak, B., Žic, T., Vrbanec, D., et al. 2013, SoPh, 285, 295
Wang, Y., Wang, B., Shen, C., Shen, F., & Lugaz, N. 2014, JGRA, 119, 5117
Wang, Y., Zhang, Q., Liu, J., et al. 2016, JGRA, 121, 7423
Wang, Y. M., Ye, P. Z., & Wang, S. 2003, JGRA, 108, 1370
Xu, M., Shen, C., Wang, Y., Luo, B., & Chi, Y. 2019, ApJL, 884, L30
Zhang, J., Richardson, I., Webb, D., et al. 2007, JGRA, 112, A10102
Zhang, T., Baumjohann, W., Delva, M., et al. 2006, P&SS, 54, 1336